Size-Dependent Shape and Tilt Transitions in In$_2$O$_3$ Nanoislands Grown on Cubic Y-Stabilized ZrO$_2$(001) by Molecular Beam Epitaxy
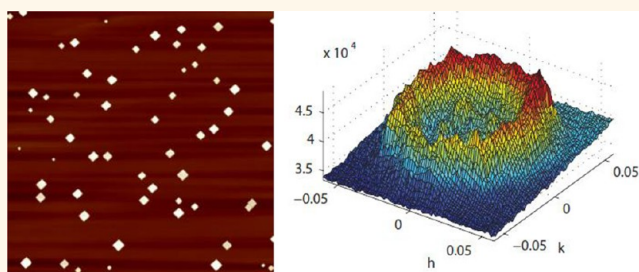
Kelvin H. L. Zhang,[†] Anne Bourlange,[†] Russell G. Egdell,[†,*] Stephen P. Collins,[‡] Richard J. Bean,[§] Ian K. Robinson,[§] and Roger A. Cowley[⊥]

[†]Inorganic Chemistry Laboratory, Department of Chemistry, University of Oxford, South Parks Road, Oxford OX1 3QR, United Kingdom, [‡]Diamond Light Source Ltd., Didcot, Oxfordshire, OX11 0DE, United Kingdom, [§]London Centre for Nanotechnology, University College London, London WC1H 0AH, United Kingdom, and [⊥]Clarendon Laboratory, Department of Physics, University of Oxford, Parks Road, Oxford OX1 3PU, United Kingdom

Transparent conducting oxides (TCOs) are key technological materials that combine high optical transmission in the visible region with a high electrical conductivity. They have widespread application as window electrodes in display devices and solar cells.[1−5] Tin-doped indium oxide (In$_2$O$_3$) is the TCO of choice in many areas of application. It is widely known as indium tin oxide or ITO and is obtained by degenerate n-type doping of In$_2$O$_3$ with Sn. Somewhat surprisingly, many of the basic physical properties of In$_2$O$_3$ itself have proven to be controversial. Thus, for many years, the band gap of indium oxide was presumed to be direct and allowed and was quoted to be around 3.75 eV. This value was established by Hamberg *et al.*[6] in 1983 from analysis of transmission data for ITO thin films. However, much earlier experiments on In$_2$O$_3$ single crystals revealed a weak optical onset at 2.69 eV,[7] which was attributed at that time to an indirect gap. Subsequent band structure calculations[8] failed to find a significant upward dispersion away from the Γ point in the topmost valence band, as required by the indirect gap hypothesis, leading to the suggestion that the weak onset was associated with defect states.[9] More recent work has established that indium oxide in fact has a direct energy gap less than 3 eV, but transitions from the top of the valence band are dipole forbidden.[10]

ITO as used in displays and other devices is usually deposited on glass or polymer substrates by sputtering techniques to give polycrystalline films. However, the possibility of development of TCO materials as the active layer in transparent optoelectronic devices has encouraged a recent surge of activity in the growth of single-crystal epitaxial TCO thin films using oxygen plasma-assisted molecular beam epitaxy (MBE).[11−17] Now that the basic physical properties of indium oxide and its surfaces are better understood, interest is evolving toward the growth and exploitation of nanostructured indium oxide epitaxial films.

ABSTRACT

The growth of In$_2$O$_3$ on cubic Y-stabilized ZrO$_2$(001) by molecular beam epitaxy leads to formation of nanoscale islands which may tilt relative to the substrate in order to help accommodate the 1.7% tensile mismatch between the epilayer and the substrate. High-resolution synchrotron-based X-ray diffraction has been used in combination with atomic force microscopy to probe the evolution in island morphology, orientation, and tilt with island size. Very small islands formed at low substrate coverage are highly strained but exhibit no tilt, while intermediate islands are tilted randomly in all directions, giving rise to distinctive doughnut-shaped structure in three-dimensional reciprocal space isosurfaces. The largest islands with lateral sizes on the order of 1 μm tilt away from the four equivalent in-plane ⟨110⟩ directions, giving three-dimensional scattering isosurfaces dominated by structure at the four corners of a square. Spatially resolved reciprocal space mapping using an X-ray beam with dimensions on the order of 1 μm suggests that the four-fold symmetry observed using a larger beam arises from averaging over an ensemble of islands, each with an individual tilt down one direction, rather than from the coexistence of differently tilted domains within a given island.

**KEYWORDS:** epitaxy · indium oxide · reciprocal space mapping · synchrotron radiation

In_2O_3 adopts a body-centered cubic bixbyite structure belonging to space group $Ia\bar{3}$ and with lattice parameter $a_e = 10.1170$ Å. The structure can be described as a $(2 \times 2 \times 2)$ superstructure of fluorite but with 1/4 of the oxygen sites left empty. By contrast, the face-centered cubic fluorite structure of Y-stabilized ZrO_2 (YSZ) belongs to the space group $Fm\bar{3}m$. The cubic lattice parameter of YSZ varies with Y doping level and is measured to be $a_s = 5.1447$ Å at the 17% Y doping level of substrates used in the current work, where the doping level $100 \times \%$ is defined by the stoichiometry parameter x in $Zr_{1-x}Y_xO_{2-x/2}$ and the subscripts in a_s and a_e denote the substrate and the epilayer, respectively. Thus, there is a mismatch m of -1.68% between $2a_s$ for YSZ (10.2894 Å) and a_e for In_2O_3 where m is defined by[18]

$$m = \frac{a_e - 2a_s}{2a_s} \times 100\%$$

For both the fluorite and bixbyite structures, the (001) surface is polar whereas the (111) and (110) surfaces are nonpolar.[19] The surface energies lie in the sequence $\gamma(001) \gg \gamma(110) > \gamma(111)$.[20,21] Epitaxial growth of In_2O_3 on YSZ(111) leads to development of continuous or near continuous thin films which are highly strained at low coverages.[22−24] By contrast, growth on (001)-oriented substrates leads to formation of striking arrays of monodisperse nanoscale square islands:[20,25] for coverages (defined in terms of the thickness that would have been obtained in a layer by layer growth mode) in excess of about 20 nm, these are all oriented with edges aligned along ⟨110⟩ directions of the substrate. This orientation allows development of low energy {111} side facets giving islands with a truncated pyramidal morphology.

Previous X-ray scattering measurements on indium oxide islands have been performed on a laboratory-based instrument. Samples were mounted with the [001] growth direction in the horizontal scattering plane together with either the [100] or [110] direction. Transverse wavevector scans through the epilayer (004) and (008) Bragg reflections gave a three-peak structure for wavevector transfers along the [110] direction but a two-peak structure when the scans were performed along the [100] direction.[26] These results suggested that the atomic planes of the islands are not parallel to those of the substrate but are tilted at an angle of about 0.7° from the four different in-plane ⟨110⟩ directions, so that in the (h,k) plane, scattering intensity is found at the four corners of a square. The observed structure was then surmised to arise because of the relatively poor vertical angular resolution of the diffractometer, so that intensity arising from momentum transfer orthogonal to the horizontal scattering plane is collected by the detector.

The tilt helps to relieve tensile strain arising from the mismatch between the epilayer and the substrate.
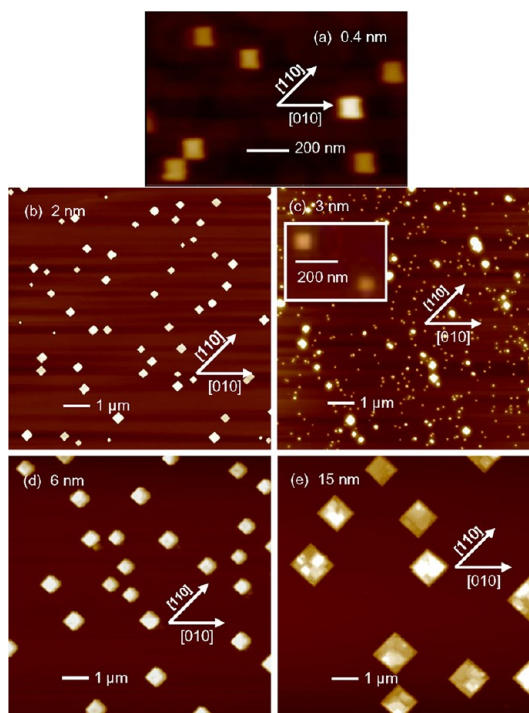
Figure 1. AFM images of (001)-oriented island epilayer samples of In_2O_3 grown on Y-ZrO_2(001) at 900 °C used in reciprocal space mapping experiments. The average thicknesses are as follows: (a) 0.4 nm, (b) 2 nm, (c) 3 nm, (d) 6 nm, (e) 15 nm. Note the difference in scale between (a) and the other panels. The inset in (c) shows an expanded view of some small islands with the same scale as in (a).

For sufficiently thin films or islands, it is anticipated that mismatch can be accommodated purely by pseudomorphic strain rather than tilt so that as a function of coverage there should be a switchover between untilted and tilted island growth.[27] Unfortunately, it was not possible to characterize the expected tilt transition in laboratory-based experiments owing to the very weak scattering found at low coverages and interference from scattering from the substrate truncation rods when mapping around (004) and (008) epilayer reflections.[26]

In the present paper, we use synchrotron-based X-ray diffraction to probe strain and tilt in epitaxial island films of In_2O_3 grown on YSZ(001) with a range of thicknesses between 0.4 and 15 nm, where thickness is defined in terms of the total volume of material contained in the islands per unit area. The morphology of the samples was characterized by atomic force microscopy (AFM). Both two-dimensional (2D) and three-dimensional (3D) diffraction data were collected, and the influence of the X-ray spot size was investigated. The experiments allow us to unravel a rich and complex pattern of behavior involving transitions in island morphology, island orientation, and island tilt as a function of surface coverage and island size.

RESULTS AND DISCUSSION

Sample Morphology. AFM images of the five samples used in the current work are shown in Figure 1.

TABLE 1. Characteristics of the Five Island Samples Studied in the Present Work

average coverage (nm)	island density (islands/μm²)	average island length (nm)	average island height (nm)	island orientation
0.4	1.95	100	20	$\langle 100 \rangle$
2	0.64	300	35	$\langle 110 \rangle$
3	4.04	90	30	$\langle 100 \rangle$
bimodal	0.36	280	65	$\langle 110 \rangle$
6	0.23	540	90	$\langle 110 \rangle$
15	0.075	1160	150	$\langle 110 \rangle$

The average film thicknesses as defined above range between 0.4 and 15 nm. It is quite clear that for all films an island growth mode is obtained. The AFM image of the sample with lowest coverage shows small square islands with typical side length on the order of 100 nm and edges aligned along $\langle 100 \rangle$ directions. With a higher coverage of 2 nm, the islands are larger and sparser with typical edge dimensions in excess of 200 nm. The edges align along $\langle 110 \rangle$ directions. The general overall trend with further increasing coverage is for the density of islands to decrease and for the size of islands to grow such that for the highest coverage studied in the present experiments the typical island size is around 1000 nm or greater (Figure 1e). This is indicative of a mechanism for island growth involving initial nucleation followed by a phase of Ostwald ripening as growth continues. Some growth runs were carried out on a batch of substrates which led to much higher island densities and a bimodal distribution of island sizes, with coexisting small islands aligned along $\langle 100 \rangle$ directions and larger islands aligned along $\langle 110 \rangle$. An AFM image for one of these samples is shown in Figure 1c. The characteristics of the five samples studied in the current work are summarized in Table 1.

The clear evolution of island alignment and island shape with size is further illustrated in Figure 2. Clusters with lateral dimensions below around 120 nm adopt a square shape with edges aligned along $\langle 100 \rangle$ directions. This allows development of {110} sloping side facets, as shown in the schematic to the right of the AFM image. Clusters with lateral dimensions in excess of about 240 nm also adopt a square shape but now with edges aligned predominantly along $\langle 110 \rangle$ directions. This now allows development of lower energy {111} side facets. Intermediate clusters with typical lateral dimensions on the order of 180 nm adopt an octagonal shape with exposure of both {110} and {111} side facets. The aspect ratio of the islands also showed a marked dependence on island size and alignment. As seen in the bottom panel of Figure 2, the height to length ratio increased with island size for the small $\langle 100 \rangle$-oriented islands, reaching a maximum value in excess of 0.4 for islands with a lateral dimension of about 100 nm. The larger $\langle 110 \rangle$-oriented islands had a lower height to length ratio which decreased to
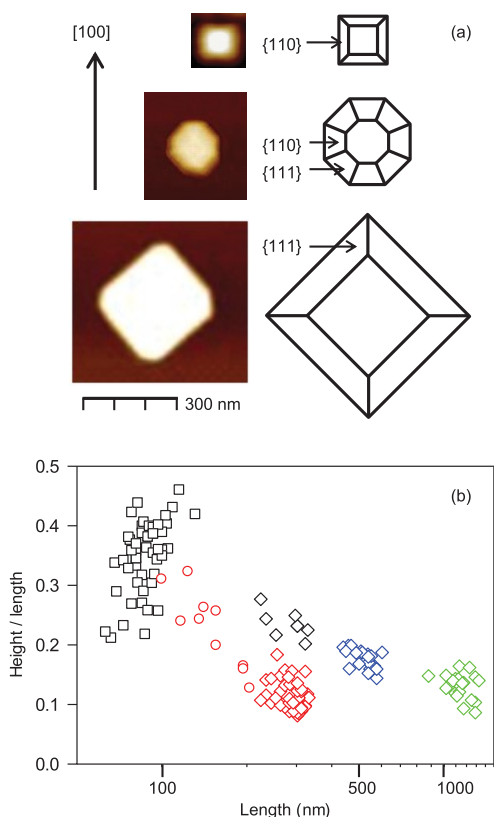

Figure 2. (a) Evolution of epilayer islands as a function of size, with schematics of the island morphology shown to the right. (b) Variation of island height/length ratio with island length presented in a plot with a logarithmic length scale and a linear height/length scale. Squares (□) represent islands with edges oriented along $\langle 100 \rangle$ directions, diamonds (◇) islands oriented along, $\langle 110 \rangle$ directions, and circles (○) octagonal islands.

around 0.1 for islands with lateral dimension on the order of 1000 nm.

Two-Dimensional Reciprocal Space Mapping Experiments. High-resolution transmission electron microscopy performed on selected island samples confirmed that the epilayer grew on the substrate with $[001]_{In_2O_3} \| [001]_{Y-ZrO_2}$ and $[010]_{In_2O_3} \| [010]_{Y-ZrO_2}$, subject to the caveat of the small tilt to be discussed below.[26] Figure 3 shows a $\theta - 2\theta$ X-ray diffraction profile for a typical sample measured in the angular range between 20 and 80° using Cu Kα radiation (λ = 1.5406 Å). The epilayer (004) and (008) reflections appear at higher angle of the substrate (002) and (004) reflections. In addition, a very weak epilayer (006) reflection may be identified. There is no nearby substrate reflection because the (003) reflection is forbidden in a face-centered cubic systems. It is therefore possible to perform reciprocal space mapping experiments on films with very low coverages using the epilayer (006) reflection, without interference from scattering from the substrate.

Figure 4 shows reciprocal space maps for the lowest coverage film (with an average thickness of 0.4 nm). The upper and lower panels correspond to transverse
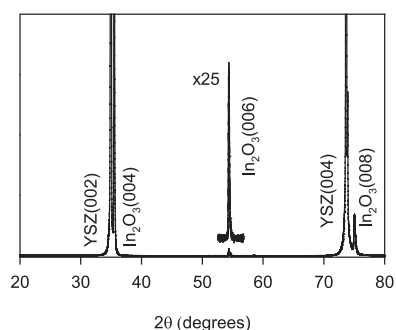
Figure 3. Typical $\theta-2\theta$ X-ray diffraction trace for In_2O_3 epilayer on Y-ZrO_2(001). Epilayer (004) and (008) peaks are found close to the substrate (002) and (004) peaks with a weak (006) substrate peak also apparent with no nearby substrate peak.
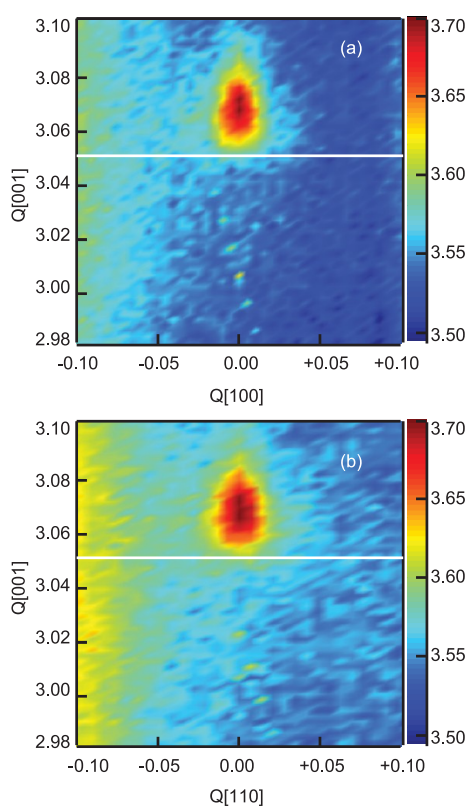
Figure 4. Two-dimensional reciprocal space maps of island epilayer sample with 0.4 nm average thickness. Wavevector transfer is given in reciprocal lattice units of the substrate with longitudinal transfer along [001] in the vertical direction. The horizontal white lines identify the value of Q[001] for unstrained In_2O_3. (a) Transverse wavevector transfer along [100] direction. (b) Transverse wavevector transfer along [110] direction.

wavevector transfer along [100] and [110] directions, respectively. The maximum in the scattering is found for zero transverse momentum transfer. This establishes that the islands found in this ultrathin film are not tilted relative to the substrate as has been found earlier for island films with nominal quoted thicknesses of 20 nm or more.[26] At the same time, there is evidence for pronounced strain in the films, and the scattered
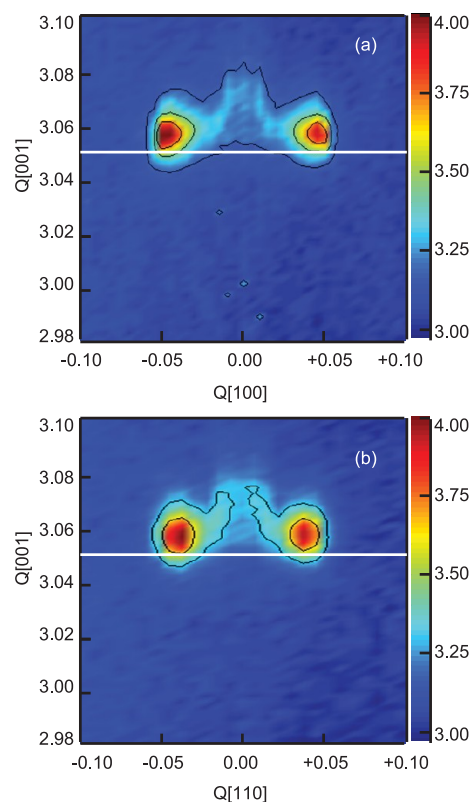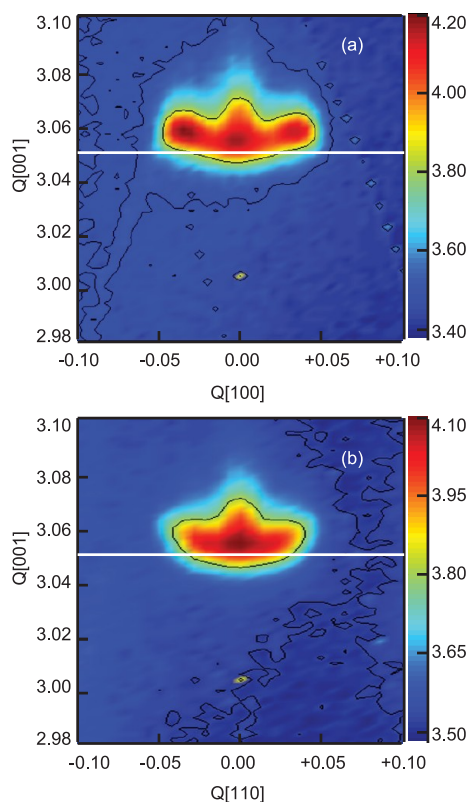

Figure 5. Two-dimensional reciprocal space maps of island epilayer sample with 6 nm thickness. Wavevector transfer is given in reciprocal lattice units of the substrate with longitudinal transfer along [001] in the vertical direction. The horizontal white lines identify the value of Q[001] for unstrained In_2O_3. (a) Transverse wavevector transfer along [100] direction. (b) Transverse wavevector transfer along [110] direction.

intensity is displaced toward higher longitudinal wavevector transfer from the value of 3.051 reciprocal lattice units anticipated for unstrained In_2O_3. This increase is associated with a decrease in the separation between atomic planes normal to the surface resulting *via* the Poisson effect from tensile strain parallel to the surface. In fact, the reciprocal space map is elongated along the [001] direction and extends almost to the value of Q[001] = 3.090 expected for a fully strained epilayer assuming a Poisson ratio of 0.27.[24] The elongated shape is suggestive of a situation where material close to the interface is highly strained with progressive strain relaxation away from the interface.

Figure 5 shows corresponding reciprocal space maps for the film with an average thickness of 6 nm. The scattering intensity now has maximum intensity in two lobes displaced away from zero transverse wavevector. The displacement is about the same for maps with transverse momentum transfer along [100] and [110] directions and corresponds to a tilt of about 0.9°. This result is different than that found in earlier mapping experiments on samples with nominal coverages of 40 and 120 nm, where the splitting between the lobes is greater along ⟨110⟩ directions than along ⟨100⟩

Figure 6. Two-dimensional reciprocal space maps of island epilayer sample with 3 nm thickness. Wavevector transfer is given in reciprocal lattice units of the substrate with longitudinal transfer along [001] in the vertical direction. The horizontal white lines identify the value of $Q[001]$ for unstrained In_2O_3. (a) Transverse wavevector transfer along [100] direction. (b) Transverse wavevector transfer along [110] direction.

directions.[26] Instead, the present results suggest that the scattering intensity in the (h,k) plane is distributed on an annulus so that the 2D reciprocal space maps are basically independent of the in-plane direction. The lobes shown in Figure 5 lie closer to $Q[001] = 3.051$ than for the more dilute sample, suggesting that the tilted islands are less highly strained than the islands of Figure 4. Finally, it is striking that weak tails of scattering intensity converge toward higher $Q[001]$ and zero $Q[100]$ or $Q[110]$. This suggests that a minority of less tilted but more strained islands coexist with the majority tilted but relatively unstrained islands: this idea is consistent with AFM images which show that in the presence of a few small ⟨100⟩-oriented islands for this sample.

Further confirmation of these conclusions is provided by mapping experiments on the sample with a bimodal distribution of island sizes. The maps for this sample are shown in Figure 6. There is clearly a superposition of structure with near zero transverse wavevector transfer (that is, $Q[100] = 0$ or $Q[110] = 0$) characteristic of untilted islands along with two lobes displaced along these directions as in Figure 5.

Three-Dimensional Reciprocal Space Mapping Experiments. Three-dimensional (3D) reciprocal space mapping

experiments were carried out on two samples prepared with average coverages of 2 and 15 nm. As shown in Figure 1, both of these samples had a rather narrow distribution of islands sizes and predominant orientation of island edges along ⟨110⟩ directions. Isosurfaces derived from a three-dimensional data set of intensity as a function of (h,k,l) around the epilayer (006) reflection are shown in Figure 7a,b. The appearance of these volume isosurfaces depends critically on the threshold value chosen. The volume plot for the 2 nm sample is composed of a doughnut-shaped feature with a mean radius of about 0.045 reciprocal lattice units, in the center of which there is weaker structure with a hint of four-fold symmetry. This central structure is displaced toward higher $Q[001]$ value than the doughnut. By contrast, the volume plot for the 15 nm sample is free of significant central structure and exhibits clear maxima in the intensity at the four corners of a square lying along ⟨110⟩ directions. An alternative and more useful way of visualizing the three-dimensional data is to integrate the intensity along the [001] direction. Figure 7c,d presents l integrated plots of this sort for the two samples. These plots clearly reveal the near circular symmetry in the (h,k) plane for the lower coverage sample and the four-fold rotational symmetry for the higher coverage sample. It thus appears that the islands in the lower coverage sample tilt randomly in all possible directions, whereas the larger islands characteristic of the higher coverage tilt preferentially along ⟨110⟩ directions, as was inferred earlier from the 2D maps of the present work and ref 26.

Spatially Resolved Investigation of Island Tilt. An obvious question arising from the previous section is whether individual islands each tilt in a specific direction, with the observed 3D intensity distribution emerging as a result of a summation over a large number of islands, or whether there are a number of differently tilted domains within a given island. To address this question, we explored the feasibility of reciprocal space mapping using a beam focused to a micrometer-sized spot on the sample using Kirkpatrick–Baez (KB) mirrors in conjunction with a variable slit mounted before the mirrors. We explored a range of slit sizes between 200 and 10 μm. The KB mirrors focus the image of the slit onto the sample. A knife edge scan was used to establish that 40 μm horizontal slits gave an effective spot size on the sample of around 6 μm so that the spot size using the smallest slits should be around 1.5 μm. Figure 8 shows l integrated (h,k) intensity plots for the 15 nm sample for a series of four different slit sizes. Reducing the slit size from 100 to 10 μm leads to a 20-fold attenuation in the l-integrated intensity, but the overall count rate remains acceptable.

There are very pronounced changes in the appearance of the (h,k) intensity plots with slit size, particularly when the slit size decreases from 20 to 10 μm. In particular,
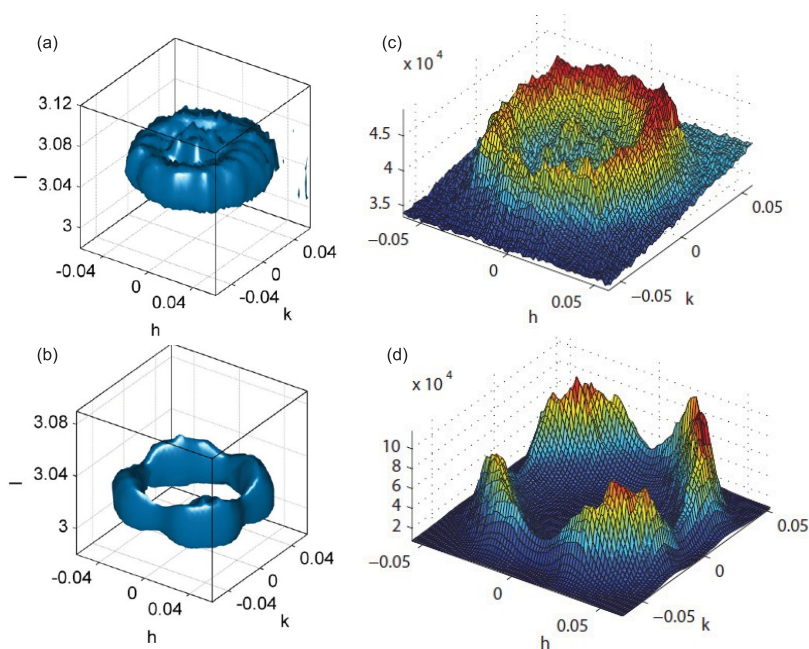
Figure 7. (a) Three-dimensional volume reciprocal space isosurface around the epilayer (006) reflection for island epilayer sample of average thickness 2 nm In_2O_3 grown on Y-ZrO_2(001) at 900 °C; (b) corresponding isosurface for 15 nm sample; (c) intensity in (h,k) plane obtained by integration of 3D (h,k,l) intensity data along l direction for sample shown in (a); (d) corresponding (h,k) intensity plot for sample with average thickness 15 nm. Wavevector transfer is given in reciprocal lattice units of the substrate and h, k, l refer to [100], [010], and [001] directions, respectively.
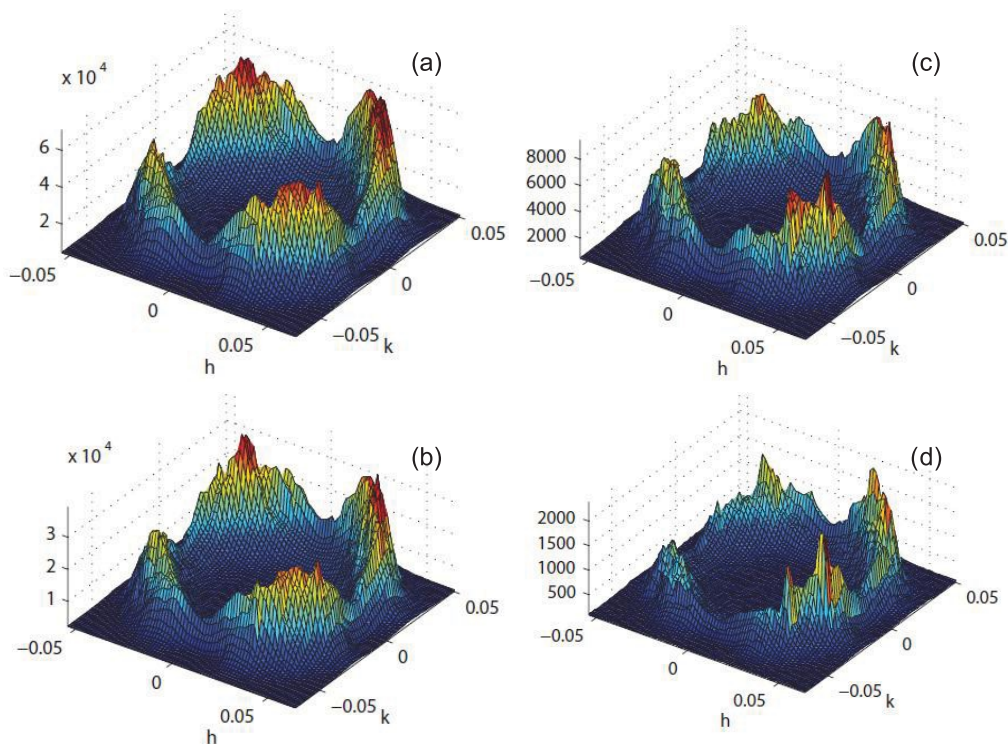
Figure 8. Intensity plots (h,k) as in Figure 7d for a series of different nominal slits before the 15 nm sample: (a) 100 μm, (b) 50 μm, (c) 20 μm, (d) 10 μm. KB mirrors focus the image of the slit onto the sample. Wavevector transfer is given in reciprocal lattice units of the substrate, and h and k refer to [100] and [010] directions, respectively.

the intensity map obtained using the smallest slits no longer displays the near four-fold symmetry found with larger slits, and scattering is very weak in one corner of the square. This is highly suggestive of reaching a limit where only a small number of islands are probed by the X-ray beam and where the sampled islands each exhibits a
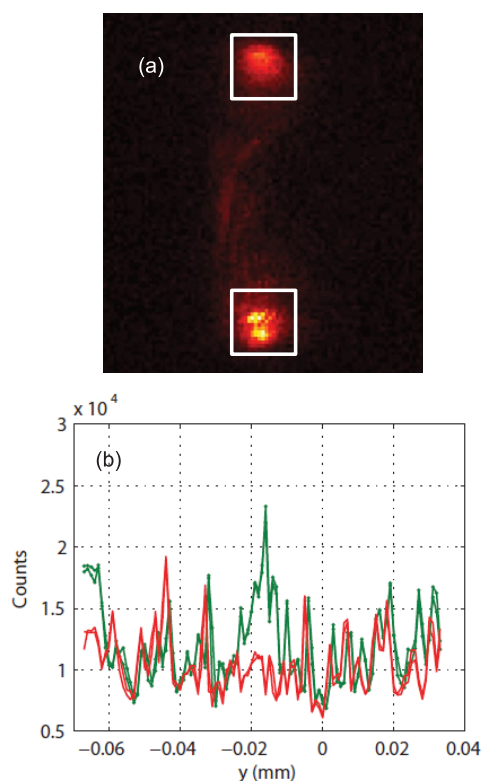
Figure 9. (a) Raw image from Pilatus area detector close to the center of an angle scan using 10 μm slits in conjunction with KB mirrors showing two features corresponding to *extrema* of the reciprocal space maps such as shown in Figure 8d. Areas used for integration of signal intensity are highlighted as white squares. (b) Variations in the integrated intensity within the two squares as the sample is translated over a range of 100 μm in 1 μm steps through the X-ray beam are shown in green and red, respectively. In each case, results from two separate lateral scans are superimposed on each other, demonstrating the excellent repeatability of the measurement.

predominant tilt in just one direction. It is also striking that the (*h,k*) plots assume an increasingly "spiky" appearance as the slit size is reduced. This is not simply related to poor signal-to-noise in the measurement, and the spiked features were found to be perfectly reproducible between successive scans. The spiked structure can be linked to distinct speckle in the raw Pilatus frames as will be discussed below. We have insufficient data to determine whether the speckle arises from coherent interference between scattering from different islands or from mosaic structure within an individual island.

To explore these ideas further, we studied the variation in intensity of the counts in a fixed Pilatus frame as the sample was translated in one direction through the X-ray beam in steps of 1 μm. Two windows were defined on the detector corresponding to different coordinates in the (*h,k*) plane (and therefore two different tilt directions), as shown in Figure 9a. The integrated intensity within each window was measured as a function of sample position. Pronounced variations in both absolute intensities within each window and in the intensity ratio between the two

windows were observed, as shown in Figure 9b. The intensity variations were highly reproducible between successive lateral scans. These observations support the conclusion that different islands each have a characteristic tilt direction and that the fluctuations in the intensity and the intensity ratio arise as individual islands move in and out of the focused X-ray beam. Further support for the conclusion is provided by the series of illustrative (*h,k*) intensity maps shown in Figures 10 and 11 for the two samples. It is obvious that the intensity distribution within the (*h,k*) map is highly sensitive to sample position in a way that would not pertain if there were multiply tilted domains within each island. The changes observed in Figure 11 are particularly striking, and by changing the sample position, it is possible to concentrate the scattered intensity in each of the four corners of the square in the (*h,k*) plane. Similarly, the (*h,k*) intensity plot for the 2 nm sample reveals that in some regions the annular structure is found whereas in others intensity is concentrated at the corners of a square.

Discussion. The experimental data discussed previously reveal three significant changes with island size. In summary:

(i) The islands evolve from having a square shape with edges aligned in ⟨100⟩ directions to orientation along ⟨110⟩ directions with increasing island size, with an intermediate regime where the islands are octagonal with exposure of both {110} and {111} side facets lying parallel to ⟨100⟩ and ⟨110⟩ directions respectively.

(ii) Small islands exhibit no tilt, whereas the largest ⟨110⟩-oriented islands with lateral dimensions of 1000 nm or greater tilt preferentially relative to ⟨110⟩ directions. Smaller ⟨110⟩-oriented islands tilt in random directions.

(iii) Small ⟨100⟩-oriented islands have a bigger height to length ratio than larger ⟨110⟩-oriented islands.

The growth morphology in a heteroepitaxial system is determined by the interplay between surface and interface energies and elastic strain energies, as well as kinetic factors. In the following, we use a simple thermodynamic approach to explain the shape and tilt transitions observed in our experiments.

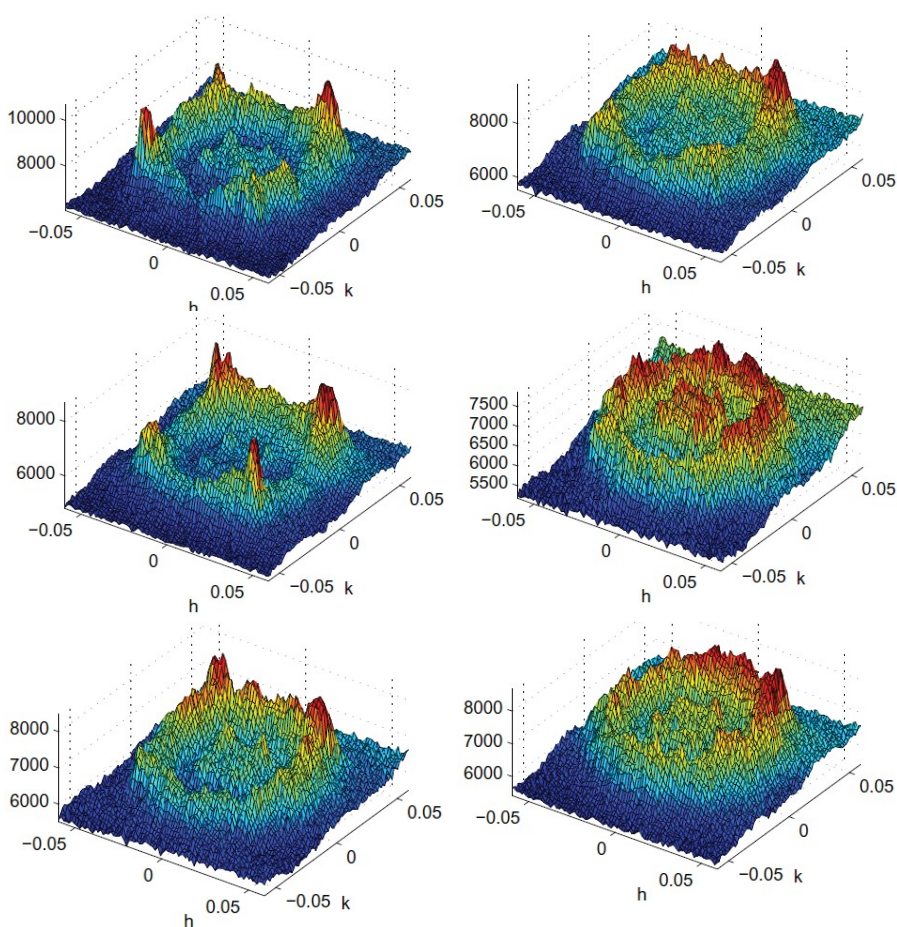Consider first the change in orientation. With corners neglected, it can be seen from Figure 12 that the sum of surface and interface energies for islands oriented with edges parallel to ⟨110⟩ directions of the substrate is given by

$$E_{\langle 110 \rangle} = 4\Gamma_1 lh + \Gamma_3 l^2$$

For an island with edges parallel to ⟨100⟩ directions we have

$$E_{\langle 100 \rangle} = 4\Gamma_2 lh + \Gamma_3 l^2$$

Figure 10. Series of (*h*,*k*) intensity plots around epilayer (006) reflection on the 2 nm sample at different points on sample surface using 20 μm slits and KB mirrors before the sample. Wavevector transfer is given in reciprocal lattice units of the substrate, and *h* and *k* refer to [100] and [010] directions, respectively.

where

$$\Gamma_1 = \gamma_e(111)\mathrm{cosec}\theta_1 - \frac{1}{2}[\gamma_s(001) + \gamma_e(001) - \gamma_i(001)]\cot\theta_1$$

$$\Gamma_2 = \gamma_e(110)\mathrm{cosec}\theta_2 - \frac{1}{2}[\gamma_s(001) + \gamma_e(001) - \gamma_i(001)]\cot\theta_2$$

$$\Gamma_3 = \gamma_i(001) + \gamma_e(001) - \gamma_s(001)$$

The γ are surface and interface energies; the subscripts e, s, and i denote the epilayer, substrate, and interface, respectively, and the numbers in brackets specify the crystal plane. The contact angle $\theta_1 = 54.7°$ for {111} side facets, while $\theta_2 = 45°$ for {110} side facets, so that the interface and facet areas are bigger for $\langle 100 \rangle$-oriented islands than for $\langle 110 \rangle$-oriented islands of a given size due to the lower slope on the side facets. When the possible influence of island orientation on the strain energy is neglected, the energy difference ΔE between the two island orientations is given by

$$\Delta E = E_{\langle 110 \rangle} - E_{\langle 100 \rangle} = 4lh(\Gamma_1 - \Gamma_2)$$

Inserting the values of surface energies for In$_2$O$_3$ from Zhang et al.,[20] which are $\gamma_e(001) = 1.759$ J m^{-2}, $\gamma_e(110) = 1.070$ J m^{-2}, $\gamma_e(111) = 0.891$ J m^{-2} along with the value $\gamma_s(001) = 1.746$ J m^{-2} for Y-ZrO$_2$

obtained by Ballabio et al.,[28] we obtain

$$\Delta E = 4lh(0.09 - 0.15\gamma_i(001))\ \mathrm{J}$$

Thus, the surface and interface energy contribution to the island reorientation energy depends critically on the interface energy: for interface energies less than 0.6 J m^{-2}, orientation with edges along $\langle 100 \rangle$ directions is favored, whereas for interface energies in excess of this value, the alternative $\langle 110 \rangle$ orientation is preferred. As will be discussed below, smaller islands are highly strained, at least in the region near the interface. For an untilted island, the strain energy is independent of orientation on a cubic (001) surface and will reduce the interface energy to a low value. By contrast, the tilt found for larger islands introduces tilt dislocations at the interface, thus increasing the effective interface energy. Qualitatively, it is therefore possible to rationalize the transition in island orientation in terms of increasing interface energy with increasing island size.

Turning next to the tilt transition, it needs to be recognized that tensile mismatch in an epitaxial system can be relieved purely by elastic strain, as shown schematically in Figure 13a,b. The resulting
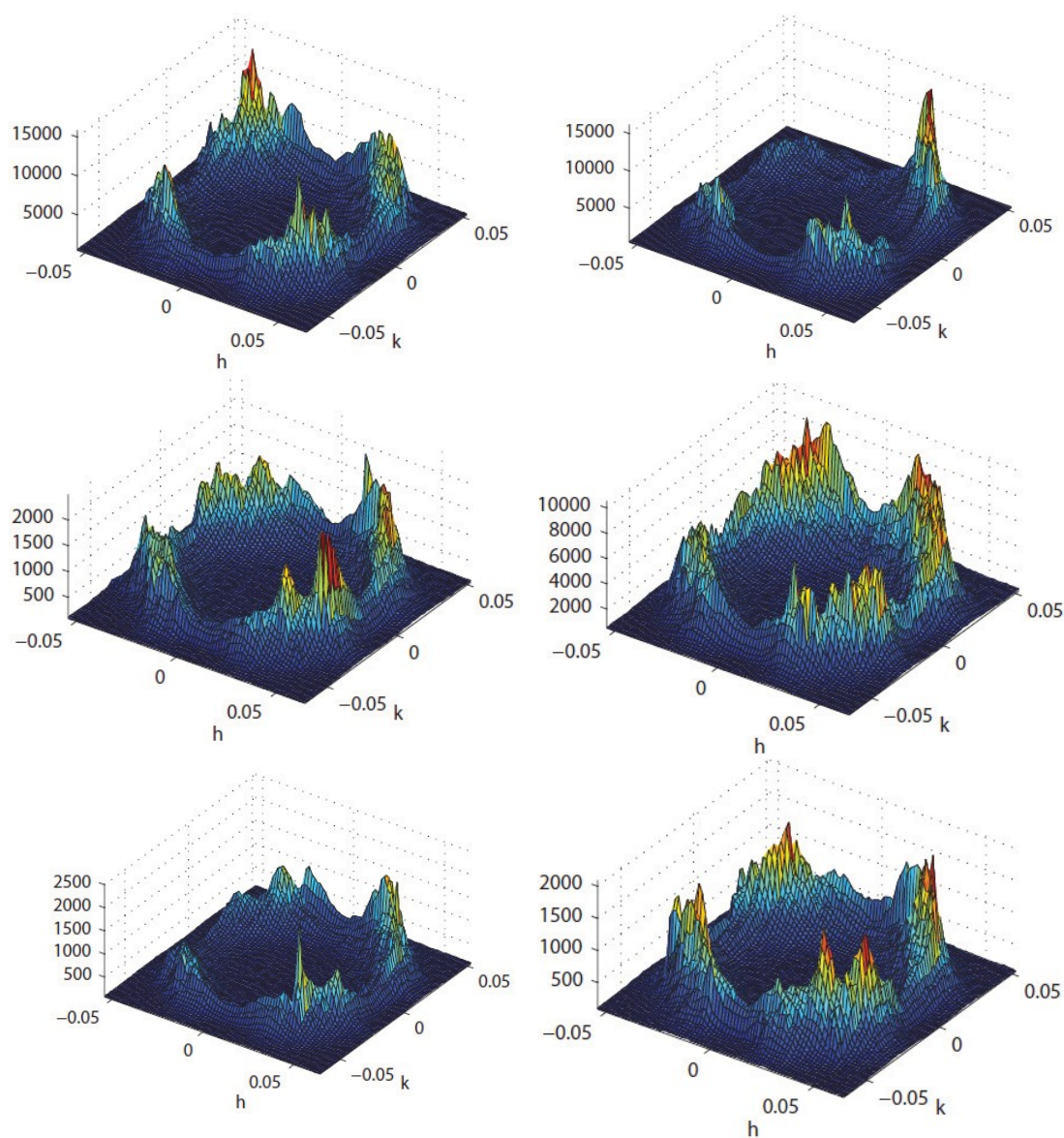
Figure 11. Series of (h,k) intensity plots around epilayer (006) reflection at different points on the 15 nm sample using 10 μm slits and KB mirrors before the sample. Wavevector transfer is given in reciprocal lattice units of the substrate, and h and k refer to [100] and [010] directions, respectively.
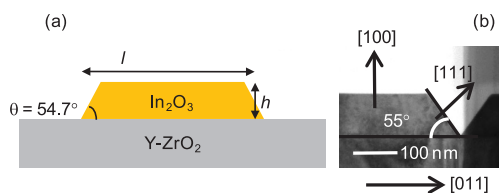
Figure 12. (a) Definition of the parameters l, h, and θ used in analysis of island orientation on (001) substrates, assuming orientation with edges parallel to $\langle 110 \rangle$ directions. (b) Detail of a cross sectional TEM image of the edge of an island grown on a (001) substrate at 900 °C viewed down the a $\langle 110 \rangle$ direction, confirming a contact angle of close to 54.7° expected for a {111} side facet.

pseudomorphic growth mode will lead to a compression of interplanar separations normal to the surface *via* the Poisson effect. Alternatively, a simple geometric construction as shown in Figure 13c shows that strain

can be relieved purely by tilt, with the consequent introduction of periodic tilt dislocations at the interface. The step heights in these dislocations are determined by the distance between adjacent cationic planes in the epilayer. For In_2O_3, this distance is $a_e/4 = 2.59$ Å. The tilt angle ψ is determined by the lattice matching factor $f = a_e/a_s$ through the expression cos $\psi = f$. Even for the very small mismatch defined by $f = 0.983$ as for the present system, relief of mismatch purely by tilt would require a rather large tilt angle $\psi = 10.6°$, assuming tilt around $\langle 100 \rangle$ directions. However, as shown in Figure 13d, coupling tilt and associated tilt dislocations with periodic misfit (*i.e.*, edge) dislocations localized at the interface allow accommodation of misfit with much smaller tilt angles. As shown by Yamada *et al.*,[27] the tilt angle in this situation is

given by

$$\tan \psi = \frac{p(1 - f^2)}{n + f\sqrt{n^2 + p(1 - f^2)}}$$

where n is the number of misfit dislocations per tilt dislocation and p is an aspect ratio which is defined by the ratio of interatomic separations normal and parallel to the surface. Assuming $n = 1$ and $p = 1$ as would pertain for tilt down $\langle 100 \rangle$ directions, we obtain $\psi = 0.97°$, while for $n = 1$ and $p = 1/\sqrt{2}$ as would pertain for tilt down $\langle 110 \rangle$ directions, one obtains $\psi = 0.68°$, which is quite close to the observed value. Yamada et al. further showed[27] that, in general, there should be a transition between untilted and tilted growth as the thickness of an epilayer increases: for sufficiently thin films, it will always be favorable to accommodate misfit by pseudomorphic strain rather than by tilt with the two sorts of dislocations localized at the interface. This explains qualitatively our observation of nontilted growth for very small islands.

The issue of tilt direction requires somewhat different considerations. Lattice tilting only helps to relieve lattice mismatch in the tilt direction. However, in a cubic system, there is biaxial mismatch. Along the in-plane direction orthogonal to the tilt direction (which is [010] for tilt along the [100] direction and [1$\bar{1}$0] for tilt along the [110] direction), the mismatch must be accommodated by lattice strain, possibly coupled with edge dislocations. This gives rise to an elastic strain energy contribution to the overall energy of an island. It is therefore necessary to take account of the relative magnitudes of the energies associated with strains along the $\langle 100 \rangle$ and $\langle 110 \rangle$ directions. The former is associated with the tilt along the $\langle 100 \rangle$ and the latter with the tilt along the $\langle 110 \rangle$ directions, respectively. Using interatomic potentials based on the Born model, the three independent elastic constants for bixbyite In_2O_3 were found to be $c_{11} = 298$ GPa, $c_{12} = 142$ GPa, and $c_{44} = 76$ GPa.[29] The energy associated with uniaxial elastic strain in $\langle 100 \rangle$ directions is determined by $c_{\langle 100 \rangle} = c_{11} = 298$ GPa. The corresponding value along the $\langle 110 \rangle$ direction is given by $c_{\langle 110 \rangle} = (2c_{11} + 2c_{12} + c_{44})/4 = 239$ GPa. Thus the strain energy associated with tilt and orthogonal strain along the $\langle 110 \rangle$ directions is approximately 20% lower than that for the $\langle 100 \rangle$ directions. The preference for tilt along $\langle 110 \rangle$ directions arising from these considerations is augmented by the fact that the easiest slip systems for ionic crystals with the fluorite structure such as CaF_2,[30] UO_2,[31] and CeO_2[32] are of the general type $\{001\}\langle 110 \rangle$. When it is assumed that the dominant slip systems for the bixbyite structure are of the same type, this favors the tilted misfit or edge dislocations shown in Figure 13 to lie in $\{110\}$ planes, as must be the case if the dislocations are to couple with tilt along $\langle 110 \rangle$ directions.
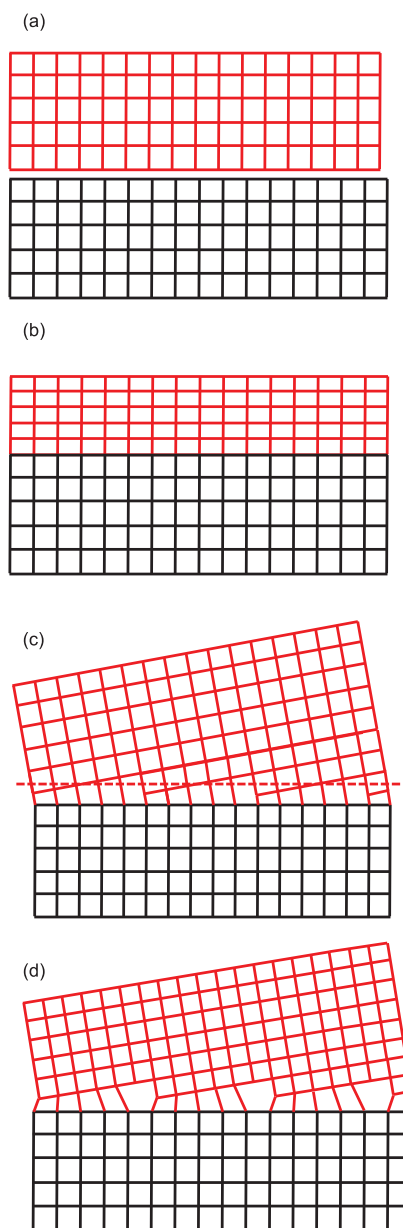
Figure 13. (a) Schematic of the interface of two cubic materials viewed down the [010] direction where the lattice parameter of the epilayer is less than that of the substrate such that $f = a_e/a_s = 0.98$. (b) Schematic of accommodation of the mismatch by elastic strain in the epilayer. The Poisson contraction normal to the surface is exaggerated. (c) Schematic of accommodation of mismatch purely by tilt. The figure shows how registry can be maintained by tilting with a tilt angle $\psi = 10.5°$ for $f = 0.98$ by the introduction of periodic tilt dislocations and a sawtooth variation of compressive and tensile strain at the interface. (d) Schematic of a more strongly mismatched interface between cubic materials as in (a) but with $f = 0.82$. Misfit is now accommodated by introduction of both tilt dislocations and periodic misfit (edge) dislocations with $n = 1$ giving a tilt angle $\psi = 9.6°$. See text for definition of n.

This simple reasoning shows that, in agreement with the experiments on large islands, lattice tilt along $\langle 110 \rangle$ directions with accompanying strain in an orthogonal $\langle 110 \rangle$ direction is favored over tilt along $\langle 100 \rangle$ directions. However, it does in itself offer an explanation

of the random tilt for smaller islands and the switchover to oriented tilt. To account for this observation, we recognize that the misfit orthogonal to the tilt direction involves strain coupled with dislocations. The interfacial dislocations accompanied by tilting are initially generated near the edges of islands, an established mechanism during Volmer−Weber island growth. The dislocations are at first randomly distributed around the periphery of the base of the islands, giving rise to the random tilt observed for the smaller ⟨110⟩-oriented islands. As further growth proceeds, these dislocations go through annihilation and multiplication processes and reorder into a square network preferentially along ⟨110⟩ directions. This leads to the tilt directed along the four equivalent in-plane ⟨110⟩ directions for large islands.

Finally, we consider why the aspect ratio of small untilted islands is different than that of the larger tilted islands. Following Müller and Kern,[33] Henry[34] has argued that in an epitaxial system which is elastically strained at the interface the height to length aspect ratio should increase with increasing island size, as is observed for the small untilted islands in the present work. Qualitatively, this can be understood by the requirement to minimize strain energy close to the interface, coupled with the fact that the crystal can relax more easily toward the top of the island. The elongation of structure in reciprocal space maps along the [001] direction for untilted islands is indicative of a situation where there is coherent strain at the interface which is progressively relaxed in moving toward the top of the island. The situation changes for tilted islands where the tilt dislocations coupled with periodic misfit dislocations effectively release strain at the interface so that as the islands grow their shapes remain self-similar with little change in the aspect ratio.

CONCLUSIONS

There has been very little previous work on tilting during mismatched epitaxial growth of oxide thin films, although the phenomenon has been studied in a wide range of other systems including Si_3N_4 on Si[35] and $ZnSe$ on Ge.[36] There are, however, clear affinities between the present diffraction experiments and those recently performed on $BiFeO_3$(001) grown on

$TbScO_3$(110) using a synchrotron beam focused down to a spot as small as 40 nm using a zone plate. This enabled tilt domains and tilt domain boundaries to be identified in poled ferroelastic thin films.[37] It is, however, more interesting to compare the present results with the well-established shape transitions in conventional semiconductor heteroepitaxial systems such as Ge or Si/Ge on Si(001)[38−40] (4% compressive mismatch for Ge) or $InAs$ on $GaAs$(001)[41] (7% compressive mismatch). In these systems, initial pseudomorphic growth of a strained wetting layer is followed by 3D island growth on top of the wetting layer in a classic Stranski−Krastanov process. The 3D islands undergo an abrupt shape transition from shallow pyramids with {105} facets to much steeper multifaceted domes as growth proceeds. The shape transition was shown to be driven by the interplay between strain energy and the surface energies associated with side facets in the pyramids and domes. One obvious difference in our results is that growth of In_2O_3 on YSZ(001) initially proceeds in Volmer−Weber (VW) growth mode, even though the mismatch is less than 2%. As we have noted previously,[20] In_2O_3 has very large anisotropy between the energies of different low index surfaces; for example, the surface energy of the (111) and (110) planes is around one-half that of (001) surfaces, compared with only around 10% anisotropy in surface energy for Ge or $InAs$. Since the total energy of an island depends on both the areas and the surface energies of its top and side facets, the formation of In_2O_3 islands becomes a way to reduce the total surface energy of the system, rather than to increase it as the case in elemental semiconductors, if low energy side facets develop. Furthermore, the height to length aspect ratio during the initial stages of growth in our study is much larger than that in pyramidal islands formed by elemental semiconductors. This is achieved without a large penalty of increased surface energy owing to the anisotropy discussed above. More generally, it should be noted that because metal oxides have large anisotropies in their surface energies, well-defined shapes are usually maintained during heteroepitaxial growth of nanoscale islands, as demonstrated by recent work on fluorite CeO_2 grown on $LaAlO_3$(001) or $SrTiO_3$(001),[42] perovskite $La_xSr_{1−x}MnO_3$ and $SrRuO_3$ grown on $SrTiO_3$-(001),[43] and spinel Mn_3O_4 again grown on $SrTiO_3$(001).[44]

EXPERIMENTAL SECTION

Indium oxide layers were grown on 1 cm × 1 cm (001)-oriented Y-stabilized ZrO_2 substrates with a nominal Y doping level of 17% (as defined by the formula $Zr_{1−x}Y_xO_{2−x/2}$ with $x = 0.17$) in an ultrahigh vacuum oxide molecular beam epitaxy (MBE) system (SVT, USA) with a base pressure of $5 \times 10^{−10}$ mbar. This incorporated liquid nitrogen cooled cryopanels, a hot lip indium effusion cell, and a radio frequency (RF) plasma oxygen atom source operated at 200 W RF power with an oxygen background pressure

of $2 \times 10^{−5}$ mbar. Substrates were held by gravity in a recessed Mo mounting plate and heated radiatively using a graphite filament. The sample temperature was measured by a chromel-alumel thermocouple mounted behind the cradle holding the sample mounting plate. Substrates were cleaned by exposure to the oxygen atom beam with a measured substrate temperature of 900 °C. The nominal deposition rate was set at 0.01 nm s$^{−1}$ using a quartz crystal monitor offset from the substrate position, but the true growth rate on the substrate was found to be 0.035 nm s$^{−1}$ at 650 °C substrate temperature, as gauged by cross sectional

transmission electron microscopy (TEM) of the continuous thin films obtained at this temperature. Films with an island morphology were grown at a higher substrate temperature of 900 °C in growth runs whose duration extended between 30 and 3×10^3 s. The sticking coefficient for In was evidently lower at the higher temperature as the coverage was lower than expected from the low-temperature deposition rate (see above).

Atomic force microscopy (AFM) images were recorded in a Digital Instruments Multimode scanning probe microscopy instrument with a Nanoscope IIIa controller operating in a contact mode as described in detail elsewhere.[12] The effective coverage in the films grown at 900 °C was obtained by dividing the total volume of islands obtained from AFM images over a defined area by that area and represents the thickness that would have been obtained in a layer-by-layer growth mode.

The $\theta-2\theta$ X-ray diffraction profiles were measured in-house using a PANalytical X'Pert Pro diffractometer incorporating a monochromated Cu Kα source ($\lambda = 1.5406$ Å). Reciprocal space mapping experiments were performed on the undulator beamline I16 on the Diamond Synchrotron in the UK using 8.000 keV photons, corresponding to $\lambda = 1.5498$ Å. The typical spot size was around 20 μm $\times$ 200 μm, although this could be reduced significantly using variable slits and a pair of Kirkpatrick−Baez (KB) mirrors mounted just before the sample position. The beamline incorporates a large 6-circle *kappa* diffractometer giving flexible access to reciprocal space. As discussed previously, most of the mapping experiments used the epilayer (006) reflection, which has no nearby substrate reflection. Initial alignment of the substrate crystal was carried out using (002) or (004) specular reflections and either (024) or (113) off-axis reflections. It was verified that off-axis reflections with doubled Miller indices of the epilayer were in the same azimuth as the substrate reflections, subject to the caveat that tilt produces small displacements in pole figure measurements, but in general, we did not collect data including both substrate and epilayer reflections owing to saturation of the detectors (see Supporting Information for a map of an off-axis reflection including both substrate and epilayer peaks).

In the first series of experiments, two-dimensional (2D) reciprocal space maps were constructed using a point detector by running a series of scans of transverse wavevector transfer, with stepping of the longitudinal wavevector transfer between successive scans. Transverse scanning was performed along both [100] and [110] directions. In later experiments, the scattering intensity was measured as a function of all three dimensions (3D) in reciprocal space using a Pilatus 100K pixel area detector. This detector captures scattered intensity on a curved surface in (h,k,l) space, and each pixel has a characteristic (h,k,l) coordinate. By scanning the angles in the scattering plane, the position of the detector surface in reciprocal space can be varied so that the scattering intensity within a large volume of reciprocal space can be mapped out very efficiently. Interpolation is then performed to give a uniform grid of intensities in reciprocal space, from which 3D isosurfaces can be derived which connect points of equal scattering intensity. In addition, reciprocal space maps around the epilayer 136 reflection were constructed for several samples but are not presented in the main body of the current paper (see Supporting Information for maps taken around off-axis reflections).

Supporting Information Available: Reciprocal space maps around epilayer (008), (006), and (226) reflections for an additional sample with average coverage of 15 nm and bimodal island size distribution. The map for the (226) reflection includes the substrate (113) reflection. Reciprocal space maps around epilayer (136) reflection for samples with average coverages of 0.4 nm, 3 nm (bimodal island size distribution), and 15 nm.

The details of these three samples are given in Table 1. This material is available free of charge *via* the Internet at http://pubs.acs.org.

REFERENCES AND NOTES

1. Granqvist, C. G.; Hultaker, A. Transparent and Conducting ITO Films: New Developments and Applications. *Thin Solid Films* **2002**, *411*, 1–5.
2. Granqvist, C. G. Transparent Conductors as Solar Energy Materials: A Panoramic Review. *Sol. Energy Mater. Sol. Cells* **2007**, *91*, 1529–1598.
3. Granqvist, C. G. Transparent Conductors for Solar Energy and Energy Efficiency: A Broad-Brush Picture. *Int. J. Nanotechnol.* **2009**, *6*, 785–798.
4. Hosono, H. Recent Progress in Transparent Oxide Semiconductors: Materials and Device Application. *Thin Solid Films* **2007**, *515*, 6000–6014.
5. Ginley, D. S.; Hosono, H.; Paine, D. C., Eds. *Handbook of Transparent Conductors*; Springer: New York, 2010.
6. Hamberg, I.; Granqvist, C. G.; Berggren, K. F.; Sernelius, B. E.; Engstrom, L. Band-Gap Widening in Heavily Sn-Doped In_2O_3. *Phys. Rev. B: Condens. Matter Mater. Phys.* **1984**, *30*, 3240.
7. Weiher, R. L.; Ley, R. P. Optical Properties of Indium Oxide. *J. Appl. Phys.* **1966**, *37*, 299–302.
8. Erhart, P.; Klein, A.; Egdell, R. G.; Albe, K. Band Structure of Indium Oxide: Indirect *versus* Direct Band Gap. *Phys. Rev. B: Condens. Matter Mater. Phys.* **2007**, *75*, 153205.
9. Gassenbauer, Y.; Schafranek, R.; Klein, A.; Zafeiratos, S.; Havecker, M.; Knop-Gericke, A.; Schlogl, R. Surface States, Surface Potentials, and Segregation at Surfaces of Tin-Doped In_2O_3. *Phys. Rev. B: Condens. Matter Mater. Phys.* **2006**, *73*, 245312.
10. Walsh, A.; Da Silva, J. L. F.; Wei, S. H.; Korber, C.; Klein, A.; Piper, L. F. J.; DeMasi, A.; Smith, K. E.; Panaccione, G.; Torelli, P.; *et al.* Nature of the Band Gap of In_2O_3 Revealed by First-Principles Calculations and X-ray Spectroscopy. *Phys. Rev. Lett.* **2008**, *100*, 167402.
11. Bourlange, A.; Payne, D. J.; Egdell, R. G.; Foord, J. S.; Edwards, P. P.; Jones, M. O.; Schertel, A.; Dobson, P. J.; Hutchison, J. L. Growth of $In_2O_3(100)$ on Y-Stabilized $ZrO_2(100)$ by O-Plasma Assisted Molecular Beam Epitaxy. *Appl. Phys. Lett.* **2008**, *92*, 092117.
12. Bourlange, A.; Payne, D. J.; Palgrave, R. G.; Foord, J. S.; Egdell, R. G.; Jacobs, R. M. J.; Schertel, A.; Hutchison, J. L.; Dobson, P. J. Investigation of the Growth of In_2O_3 on Y-Stabilized $ZrO_2(100)$ by Oxygen Plasma Assisted Molecular Beam Epitaxy. *Thin Solid Films* **2009**, *517*, 4286–4294.
13. Morales, E. H.; He, Y. B.; Vinnichenko, M.; Delley, B.; Diebold, U. Surface Structure of Sn-Doped In_2O_3 (111) Thin Films by STM. *New J. Phys.* **2008**, *10*, 125030.
14. Morales, E. H.; Diebold, U. The Structure of the Polar Sn-Doped Indium Oxide (001) Surface. *Appl. Phys. Lett.* **2009**, *95*, 253105.
15. Bierwagen, O.; White, M. E.; Tsai, M. Y.; Speck, J. S. Plasma-Assisted Molecular Beam Epitaxy of High Quality In_2O_3-(001) Thin Films on Y-Stabilized $ZrO_2(001)$ Using In as an Auto Surfactant. *Appl. Phys. Lett.* **2009**, *95*, 262105.
16. Bierwagen, O.; Speck, J. S. High Electron Mobility In_2O_3-(001) and (111) Thin Films with Nondegenerate Electron Concentration. *Appl. Phys. Lett.* **2010**, *97*, 072103.
17. Zhang, K. H. L.; Payne, D. J.; Palgrave, R. G.; Lazarov, V. K.; Chen, W.; Wee, A. T. S.; McConville, C. F.; King, P. D. C.; Veal, T. D.; Panaccione, G.; *et al.* Surface Structure and Electronic Properties of $In_2O_3(111)$ Single-Crystal Thin Films Grown on Y-Stabilized $ZrO_2(111)$. *Chem. Mater.* **2009**, *21*, 4353–4355.
18. Chambers, S. A. Epitaxial Growth and Properties of Thin Film Oxides. *Surf. Sci. Rep.* **2000**, *39*, 105–180.
19. Tasker, P. W. Stability of Ionic-Crystal Surface. *J. Phys. C: Solid State Phys.* **1979**, *12*, 4977–4984.
20. Zhang, K. H. L.; Walsh, A.; Catlow, C. R. A.; Lazarov, V. K.; Egdell, R. G. Surface Energies Control the Self-Organization of Oriented In_2O_3 Nanostructures on Cubic Zirconia. *Nano Lett.* **2010**, *10*, 3740–3746.

21. Walsh, A.; Catlow, C. R. A. Structure, Stability and Work Functions of the Low Index Surfaces of Pure Indium Oxide and Sn-Doped Indium Oxide (ITO) from Density Functional Theory. *J. Mater. Chem.* **2010**, *20*, 10438–10444.

22. Walsh, A.; Catlow, C. R. A.; Zhang, K. H. L.; Egdell, R. G. Control of the Band-Gap States of Metal Oxides by the Application of Epitaxial Strain: The Case of Indium Oxide. *Phys. Rev. B: Condens. Matter Mater. Phys.* **2011**, *83*, 161202.

23. Zhang, K. H. L.; Lazarov, V. K.; Veal, T. D.; Oropeza, F. E.; McConville, C. F.; Egdell, R. G.; Walsh, A. Thickness Dependence of the Strain, Band Gap and Transport Properties of Epitaxial In$_2$O$_3$ Thin Films Grown On Y-Stabilised ZrO$_2$-(111). *J. Phys.: Condens. Matter* **2011**, *23*, 334211.

24. Zhang, K. H. L.; Regoutz, A.; Palgrave, R. G.; Payne, D. J.; Egdell, R. G.; Walsh, A.; Collins, S. P.; Wermeille, D.; Cowley, R. A. Determination of the Poisson Ratio of (001) and (111) Oriented Thin Films of In$_2$O$_3$ by Synchrotron-Based X-ray Diffraction. *Phys. Rev. B: Condens. Matter Mater. Phys.* **2011**, *84*, 233301.

25. Bourlange, A.; Payne, D. J.; Jacobs, R. M. J.; Egdell, R. G.; Foord, J. S.; Schertel, A.; Dobson, P. J.; Hutchison, J. L. Growth of Microscale In$_2$O$_3$ Islands on Y-Stabilized Zirconia(100) by Molecular Beam Epitaxy. *Chem. Mater.* **2008**, *20*, 4551–4553.

26. Cowley, R. A.; Bourlange, A.; Hutchison, J. L.; Zhang, K. H. L.; Korsunsky, A. M.; Egdell, R. G. Tilting During Island Growth of In$_2$O$_3$ on Y-Stabilized ZrO$_2$(001) Revealed by High-Resolution X-ray Diffraction. *Phys. Rev. B: Condens. Matter Mater. Phys.* **2010**, *82*, 165312.

27. Yamada, A.; Fons, P. J.; Hunger, R.; Iwata, K.; Matsubara, K.; Niki, S. Static Analysis of Off-Axis Crystal Film Growth onto a Lattice-Mismatched Substrate. *Appl. Phys. Lett.* **2001**, *79*, 608–610.

28. Ballabio, G.; Bernasconi, M.; Pietrucci, F.; Serra, S. *Ab Initio* Study of Yttria-Stabilized Cubic Zirconia Surfaces. *Phys. Rev. B: Condens. Matter Mater. Phys.* **2004**, *70*, 075417.

29. Walsh, A.; Catlow, C. R. A.; Sokol, A. A.; Woodley, S. M. Physical Properties, Intrinsic Defects, and Phase Stability of Indium Sesquioxide. *Chem. Mater.* **2009**, *21*, 4962–4969.

30. Munoz, A.; Dominguezrodriguez, A.; Castaing, J. Slip Systems and Plastic Anisotropy in CaF$_2$. *J. Mater. Sci.* **1994**, *29*, 6207–6211.

31. Parfitt, D. C.; Bishop, C. L.; Wenman, M. R.; Grimes, R. W. Strain Fields and Line Energies of Dislocations in Uranium Dioxide. *J. Phys.: Condens. Matter* **2010**, *22*, 175004.

32. Sayle, T. X. T.; Inkson, B. J.; Karakoti, A.; Kumar, A.; Molinari, M.; Mobus, G.; Parker, S. C.; Seal, S.; Sayle, D. C. Mechanical Properties of Ceria Nanorods and Nanochains; the Effect of Dislocations, Grain-Boundaries and Oriented Attachment. *Nanoscale* **2011**, *3*, 1823–1837.

33. Muller, P.; Kern, R. Equilibrium Nano-Shape Changes Induced by Epitaxial Stress (Generalised Wulf-Kaishew Theorem). *Surf. Sci.* **2000**, *457*, 229–253.

34. Henry, C. R. Morphology of Supported Nanoparticles. *Prog. Surf. Sci.* **2005**, *80*, 92–116.

35. Dodson, B. W.; Myers, D. R.; Datye, A. K.; Kaushik, V. S.; Kendall, D. L.; Martineztovar, B. Asymmetric Tilt Boundaries and Generalized Heteroepitaxy. *Phys. Rev. Lett.* **1988**, *61*, 2681–2684.

36. Kleiman, J.; Park, R. M.; Mar, H. A. On Epilayer Tilt in ZnSe/Ge Heterostructures Prepared by Molecular-Beam Epitaxy. *J. Appl. Phys.* **1988**, *64*, 1201–1205.

37. Hruszkewycz, S. O.; Folkman, C. M.; Highland, M. J.; Holt, M. V.; Baek, S. H.; Streiffer, S. K.; Baldo, P.; Eom, C. B.; Fuoss, P. H. X-ray Nanodiffraction of Tilted Domains in a Poled Epitaxial BiFeO$_3$ Thin Film. *Appl. Phys. Lett.* **2011**, *99*, 232903.

38. Medeiros-Ribeiro, G.; Bratkovski, A. M.; Kamins, T. I.; Ohlberg, D. A. A.; Williams, R. S. Shape Transition of Germanium Nanocrystals on a Silicon (001) Surface from Pyramids to Domes. *Science* **1998**, *279*, 353–355.

39. Ross, F. M.; Tersoff, J.; Tromp, R. M. Coarsening of Self-Assembled Ge Quantum Dots on Si(001). *Phys. Rev. Lett.* **1998**, *80*, 984–987.

40. Ross, F. M.; Tromp, R. M.; Reuter, M. C. Transition States between Pyramids and Domes during Ge/Si Island Growth. *Science* **1999**, *286*, 1931–1934.

41. Kratzer, P.; Liu, Q. K. K.; Acosta-Diaz, P.; Manzano, C.; Costantini, G.; Songmuang, R.; Rastelli, A.; Schmidt, O. G.; Kern, K. Shape Transition during Epitaxial Growth of InAs Quantum Dots on GaAs(001): Theory and Experiment. *Phys. Rev. B: Condens. Matter Mater. Phys.* **2006**, *73*, 205347.

42. Gibert, M.; Puig, T.; Obradors, X.; Benedetti, A.; Sandiumenge, F.; Huhne, R. Self-Organization of Heteroepitaxial CeO$_2$ Nanodots Grown from Chemical Solutions. *Adv. Mater.* **2007**, *19*, 3937–3942.

43. Ruzmetov, D.; Seo, Y.; Belenky, L. J.; Kim, D. M.; Ke, X. L.; Sun, H. P.; Chandrasekhar, V.; Eom, C. B.; Rzchowski, M. S.; Pan, X. Q. Epitaxial Magnetic Perovskite Nanostructures. *Adv. Mater.* **2005**, *17*, 2869–2872.

44. Bogle, K. A.; Anbusathaiah, V.; Arredondo, M.; Lin, J. Y.; Chu, Y. H.; O'Neill, C.; Gregg, J. M.; Castell, M. R.; Nagarajan, V. Synthesis of Epitaxial Metal Oxide Nanocrystals *via* a Phase Separation Approach. *ACS Nano* **2010**, *4*, 5139–5146.